Deformation and Residual Stress Characteristics of TC17 Alloy Subjected to Laser Shock Peening with Single and Double Sides

IOP Conf. Series: Materials Science and Engineering **493** (2019) 012001 doi:10.1088/1757-899X/493/1/012001

Deformation and Residual Stress Characteristics of TC17 Alloy Subjected to Laser Shock Peening with Single and Double Sides

Minghuang Zhao, Chenghong Duan, Jiayi Li and Xiangpeng Luo*

School of mechanical and electrical engineering, Beijing University of Chemical Technology, Beijing 100000, China

*Corresponding author e-mail: xpluo@mail.buct.edu.cn

Abstract. Laser shock peening is a new and high technology with application value and development prospect. It can effectively improve the fatigue resistance, wear resistance and corrosion resistance of metal materials. In this paper, two-phase titanium alloy TC17, which is widely used in aerospace field, is studied by finite element method. The effects of different laser shock paths on the deformation and residual stress distribution of materials are studied. The results show that the large-area complex path strategy laser shock peening has a certain influence on the deformation and residual stress of TC17. Single-sided, double-sided simultaneous and double-sided non-simultaneous laser shock peening have a great influence on the residual stress size and distribution. Reciprocating path laser shock peening provides less distortion and higher residual stress than a zigzag path.

1. Introduction

TC17 is a dual-phase titanium alloy with high yield strength and good fracture toughness. It is mainly used to manufacture aero engine blades, fan blade disks, centrifugal impellers and other parts. Foreign body damage and fatigue damage seriously threaten the safe life of the engine. Laser Shock Peening (LSP), as a flexible and clean surface treatment technology, can effectively improve the fatigue resistance, wear resistance and corrosion resistance of metal materials [1-5].

LSP is a technique for surface modification of materials by strong shock waves generated by strong and short pulsed laser beams and substances. The short-pulse and high-energy laser beam is used to irradiate the absorbing layer coated on the surface of the part, and the absorbing layer absorbs the laser energy to rapidly generate plasma gasification, and the formed high-temperature (>10^4K) and high-pressure (>1GPa) plasmon is further accelerated. It absorbs more laser energy and further forms high-pressure (GPa-class) shock waves, which can cause high-speed plastic strain of surface materials, causing lattice distortion, dislocations, dislocation interlacing, dislocation walls, grain refinement and other micro textures. Changes, residual compressive stress on the surface of the part, to achieve surface peening or precision forming of the part [6-9]. Residual compressive stress increases the fatigue strength of the material by reducing the tensile stress level of the component to reduce the average stress, reduce the crack growth rate and even close the crack [10]. In 2008, Warren et al. [11] established a relatively simple spot matrix model to study the effect of laser shock on residual stress. Later, Hfaiedh et al. [12] established a finite element model of phase 5×5 spot matrix positive quadrilateral prism, focusing on

the influence of different shock path strategies on residual stress. In addition, recent studies [13-18] analyzed the influence of shock path strategy on the distribution of residual stress field during large-area laser shock, and can obtain better fatigue life by optimizing the shock path of metal materials. However, the above simulation model has relatively simple structure, mostly small dog bone specimens, and the path strategy is relatively simple, and the number of shocks is limited, which does not reflect the influence of large-area LSP on three-dimensional specimens.

In this paper, the finite element analysis software ABAQUS is used to simulate the LSP of TC17 titanium alloy. Three kinds of shock strategies are used to carry out single-sided shock, double-sided simultaneous shock and double-sided non-simultaneous shock, and analyze its deformation and residual stress. In the case, the system studied the effect of complex path strategy LSP on the surface properties of TC17 titanium alloy.

2. Finite element model

2.1. Analysis model

The analysis model size is 80mm×30mm×2mm, and the C3D8R solid reduction integral element is used for meshing. The test piece is divided into two parts: the shock area part and the middle part, and the two parts are connected by binding. After the grid sensitivity measurement, the cell grid sizes of the two parts were 0.15 mm × 0.15 mm × 0.15 mm and 0.5 mm × 0.5 mm × 1 mm, respectively, as shown in Figure 1(a). The 30 mm×10 mm area at the lower end of the model is the clamping part, and there are three specific laser shock strategies, as shown in Figure 1 (b). The strategy 1 shows the linear reciprocating path shock is performed on the left and right sides, and the upper part is subjected to a zigzag path shock. The strategy 2 shows, in contrast to the strategy 1, the left and right sides are subjected to a zigzag path shock, and the upper part is subjected to a linear reciprocating path shock. The strategy 3 shows a linear reciprocating path shock over the entire shock region. Each of the three strategies only shock once, and there are 471 shock points. The diameter of the circular spot is 2 mm and the spot overlap ratio is 50%.

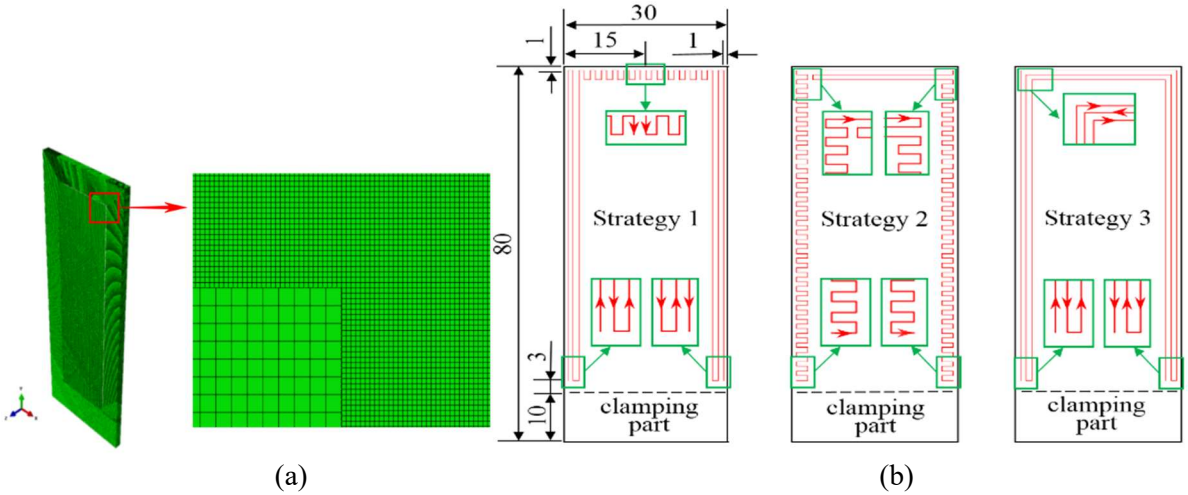

Figure 1. The established finite element model (a) and laser shock strategies (b).

2.2. Analysis process

LSP has the characteristics of high strain rate and high nonlinearity, which belongs to the category of transient shock dynamics [19]. In ABAQUS, such problems are generally calculated using a display integration algorithm, but in view of the fact that the material will generate a large amount of elastic strain during shock processing, a rebound analysis is required. There are two main methods of analysis. The first one is ABAQUS/Explicit only. This method is relatively easy, but it takes a long time to

calculate. The second is to use two modules, ABAQUS/Explicit and ABAQUS/Standard. The results of the two methods were found to be similar [20]. In order to improve the calculation efficiency, the second method is adopted in this paper. The specific process is shown in Figure 2.

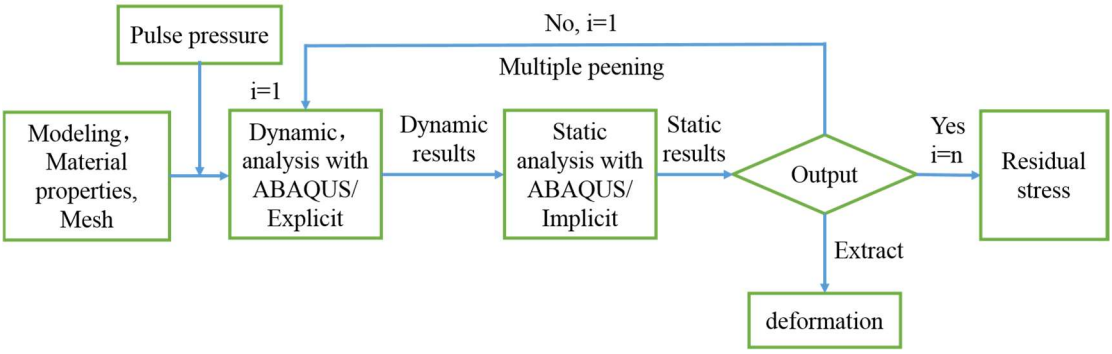

Figure 2. Finite element analysis process.

2.3. Key issue

2.3.1. Material properties. The classic Johnson-Cook (J-C) model is used to describe the dynamic response of the material [21], as in equation (1):

$$\sigma_Y = \left(A + B\varepsilon^n\right)\left(1 + C\ln\frac{\dot{\varepsilon}}{\dot{\varepsilon}_0}\right)\left[1 - \left(\frac{T - T_0}{T_m - T_0}\right)^m\right] \tag{1}$$

Among them, σ_Y is the yield stress of the material, strain peening characteristics of the A, B, C, and n reaction materials, m reaction temperature softening effect, T is the shock temperature, T_0 is the room temperature, and Tm is the melting point of the material. The elastic modulus of the material is determined by standard static tensile test, and other relevant parameters are obtained by reference [22]. The specific values are shown in Table 1.

Table 1. J-C model parameters.

parameter	density ρ, kg/m^3	Poisson's ratio v	Elastic Modulus E, MPa	A, MPa	B, MPa	n	m	C	Melting point T_m, °C
Value	4680	0.33	115813	1100	590	0.41	0.833	0.0152	1675

The material damping is calculated according to equation (2), in which the first two natural frequencies are obtained by modal calculation. The specific damping calculation values are shown in Table 2.

$$\zeta = \frac{\alpha}{2\omega_1} + \frac{\beta\omega_1}{2} = \frac{\alpha}{2\omega_2} + \frac{\beta\omega_2}{2} \tag{2}$$

Table 2. Material damping of different thickness CT specimens.

Thickness, mm	1.2	4	6	8	10	15
α	1971.952	1965.342	1955.802	1641.937	1297.485	847.011
β	4.47441^{-7}	4.50093^{-7}	4.52508^{-7}	5.37187^{-7}	6.79875^{-7}	1.04317^{-6}

2.3.2. Shock pressure model. The shock pressure model used in this paper is Fabbro model [23], and the formula for estimating the peak pressure of laser shock is:

$$P_{\max}(GPa) = 0.01\sqrt{\frac{\alpha}{2\alpha+3}}\sqrt{Z(g\cdot cm^{-2}\cdot s^{-1})}\sqrt{I\ (GW/cm^2)} \tag{3}$$

The peak value of shock pressure can be obtained according to the relevant test parameters. According to Yao's research [24], the variation rule of laser shock processing pressure with time and space is:

$$p(r,t) = p(t)\exp(-\frac{r^2}{2R^2}) \tag{4}$$

Where r is the radial distance from the arbitrary position of the shock region to the center of the spot, $p(t)$ is the change process of the shock pressure with time. $\exp(-r^2/2R^2)$ is the spatial distribution characteristics. This pressure wave spatial distribution model will be used for loading. The pulse pressure wave time distribution model is shown in Figure 3. The pulse width is 3 times the laser pulse width, namely 45ns.

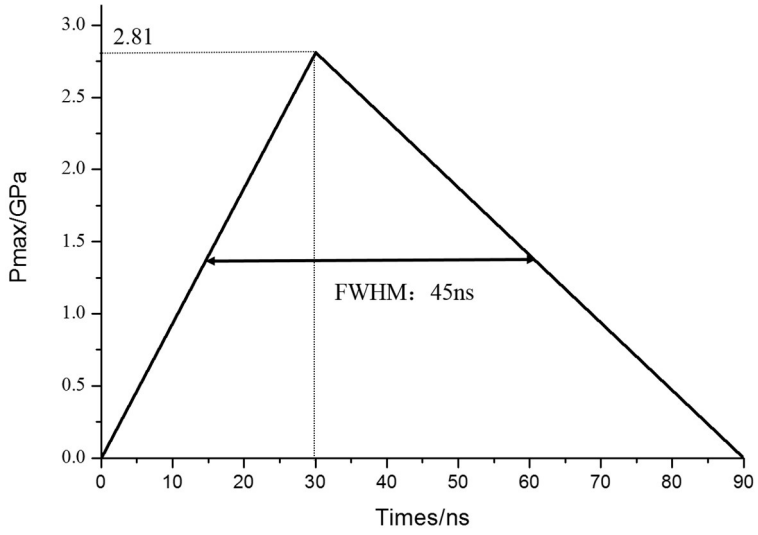

Figure 3. Peak pressure time curve of shock wave.

3. Results analysis and discussion

3.1. Single-sided shock

3.1.1. Deformation under different strategies of single-sided shock. Figure 4 is a simulation result of the deformation U3 after the three types of specimens are magnified 10 times along the Z axis. The maximum deformations of Strategy 1, Strategy 2, and Strategy 3 are 1.091mm, 1.070mm, and 1.098mm, respectively. Comparing the three sets of data, the maximum deformation of strategy 1 and strategy 3 is relatively close, and strategy 2 is slightly smaller.

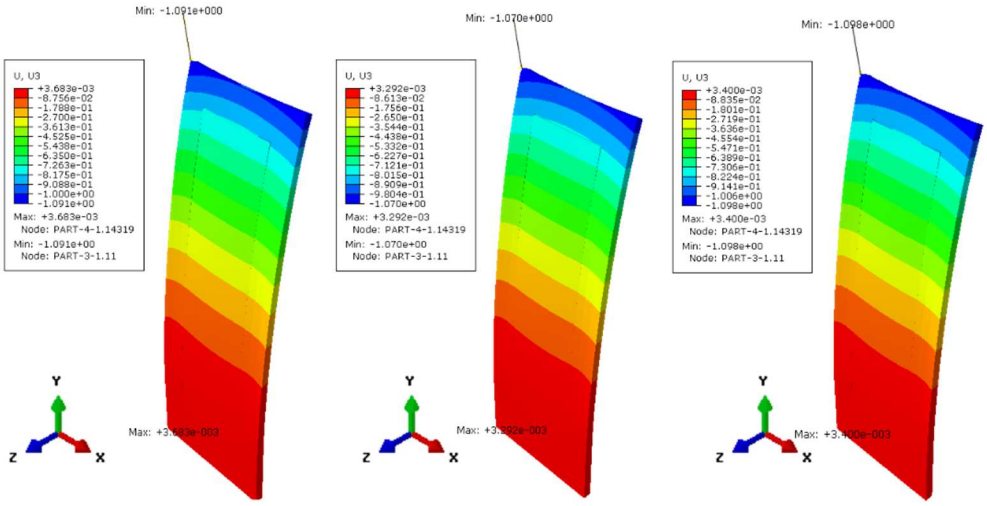

Figure 4. Z-axis deformation diagram under (a) Strategy 1, (b) Strategy 2, (c) Strategy 3.

Figure 5 shows the paths built and Figure 6 shows the displacement curves of Path 1-Path 3 under different strategies. As can be seen, the U3 of the strategy 3 is the largest, the strategy is the first time, and the strategy 2 is the smallest. However, since the three strategies of the single-sided shock generate a large deformation U3, the deformation difference between the three strategies is negligible.

3.1.2. Residual stress under different strategies of single-sided shock. Figure 7(a) is a simulation result of the residual stress S11 in the single strategy shock of the three strategies, Figure 7(b) is an enlarged result of the maximum residual stress S11, and Figure 8 is a residual manner in the thickness direction of the middle section of the model in three ways. Stress S11 simulation results. It can be seen from the above results that residual stress is generated on the upper surface and the lower surface of the model. In the thickness direction, the upper and lower surfaces are residual compressive stress, and the middle is the residual tensile stress (generated by the self-balance of the internal stress of the model), but the residual stress value of the upper surface is much larger than the lower surface. This difference is due to the single the shock wave of the surface shock is gradually attenuated during the propagation and is caused by reflection on the lower surface.

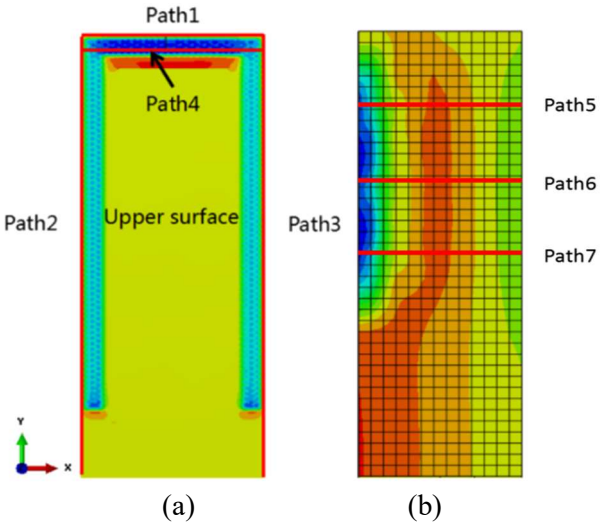

Figure 5. Schematic diagram of the paths (a) Upper surface path, (b) Intermediate section path.

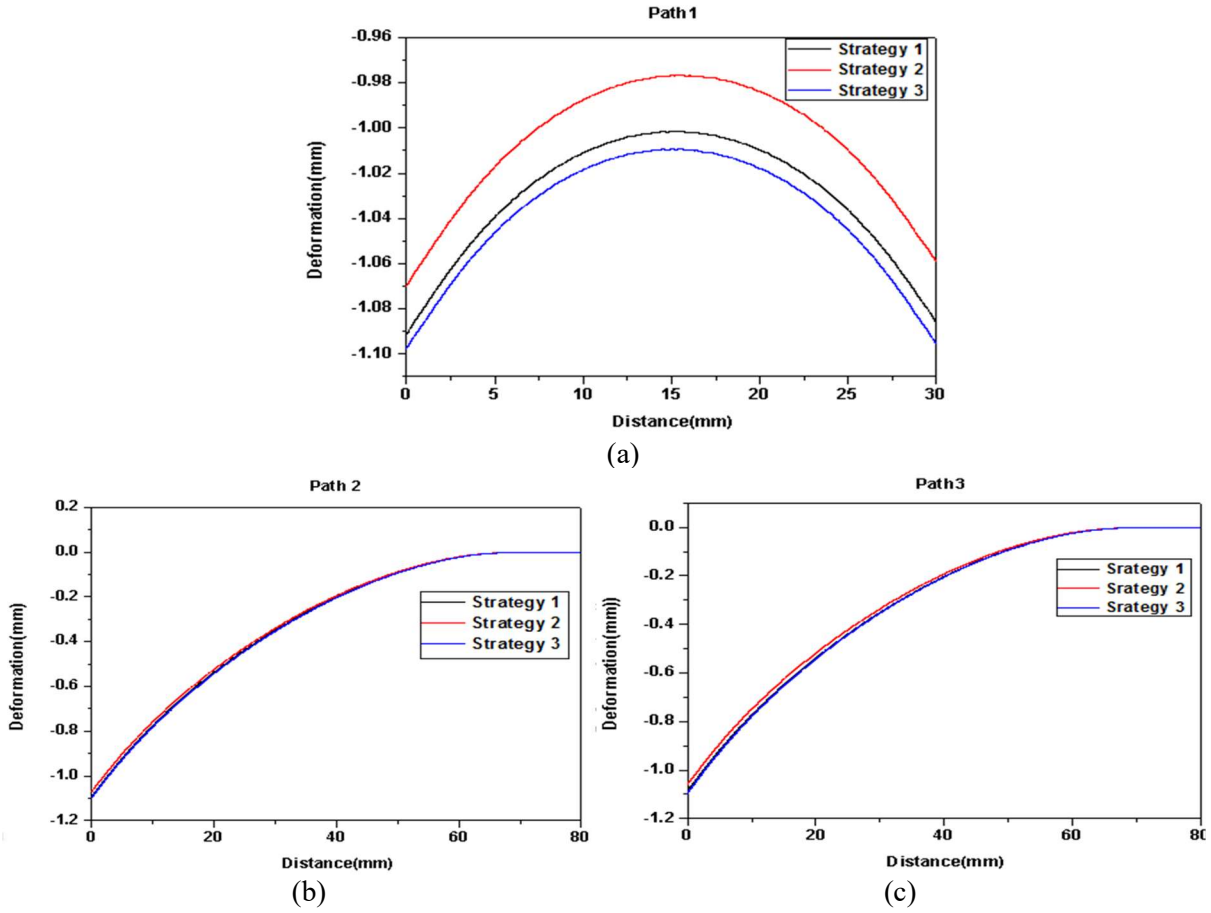

Figure 6. Displacement curve of (a) Path 1, (b) Path 2 and (c) Path 3 under different strategies.

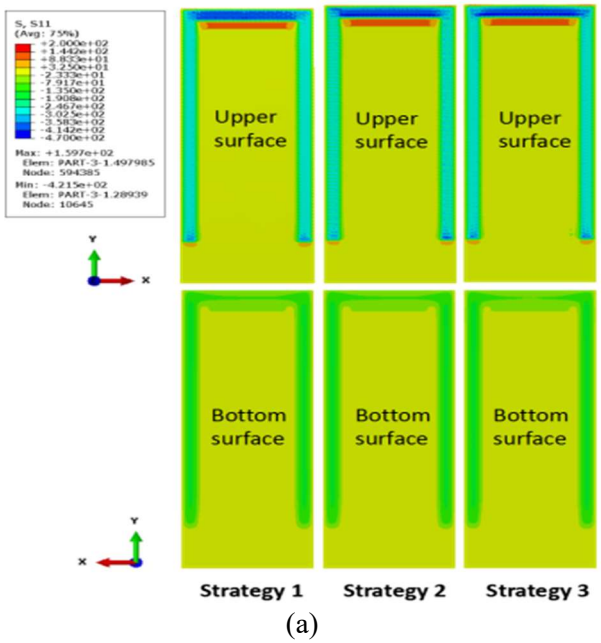

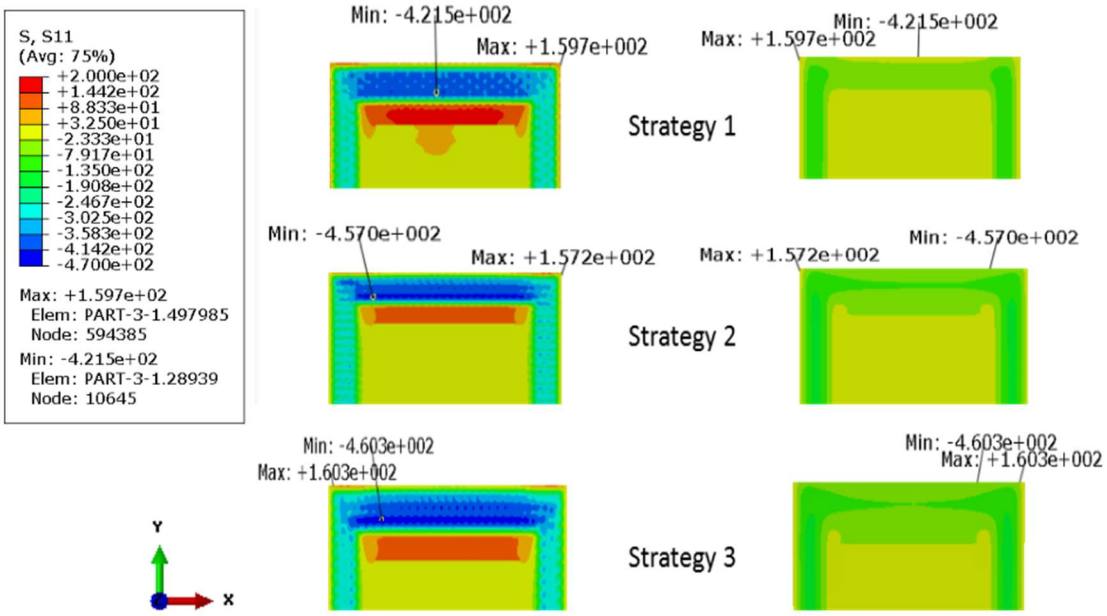

(b)

Figure 7. Residual stress S11 distribution on single side shock (a) Overall view, (b) Partial view.

As can be seen from Figure 8, the large residual compressive stress (the blue region on the left side) varies in the thickness direction. The closer the shock point is to the center of the model, the greater the residual compressive stress affects the depth.

Figure 9 is a graph showing the residual stress of Path 4 in three strategies. It can be seen from Figure 9 that the waveforms of strategy 2 and strategy 3 are similar and the waveform is relatively stable, while the strategy 1 is smaller than the lower value and the waveform is not regular. This shows that the zigzag shock strategy of the upper part of the model significantly affects the shock area. The residual stress distribution is affected by the shock of adjacent shock points in a short time, and the residual stress distribution is more irregular.

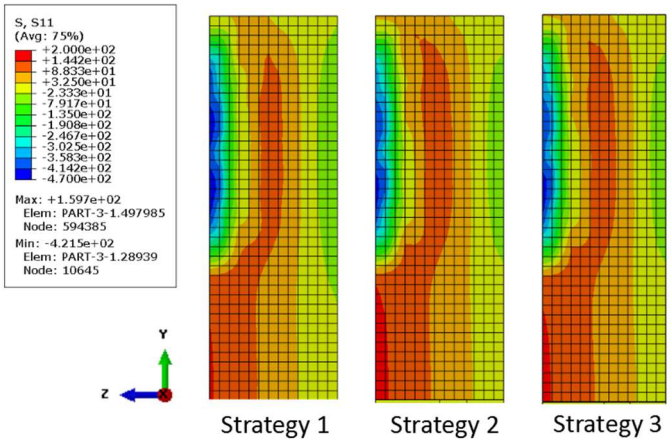

Figure 8. The distribution of the residual stress S11 in the middle section of the model in three strategies along the thickness direction.

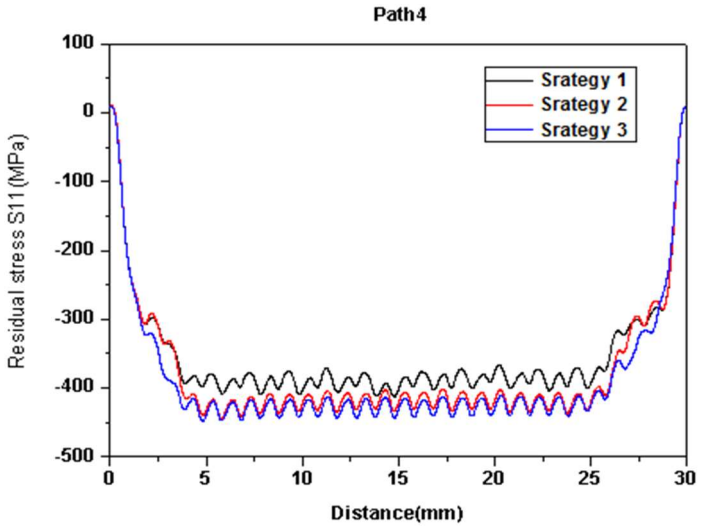

Figure 9. Residual stress curve of Path 4 in three strategies.

Table 3. Residual stress values of Path 5-Path 7 under different strategies.

Path	5			6			7		
Strategies	1	2	3	1	2	3	1	2	3
Residual stress on the upper surface (MPa)	-360	-341	-344	-386	-390	-395	-401	-420	-430
Residual stress on the lower surface (MPa)	-62	-63	-62	-79	-80	-79	-71	-73	-71
Maximum residual tensile stress (MPa)	78	82	81	90	90	91	88	89	89

Table 3 shows the residual stress values of Path 5-Path 7 under different strategies. It can be seen that the residual tensile stress induced by the three methods is not much different, and the residual compressive stress induced by the two methods is not much different. The maximum residual of the three methods is compared with the areas near Path 6 and Path 7 with large residual compressive stress. Compressive stress, Strategy 3>Strategy 2>Strategy 1.

3.2. Double-sided simultaneous shock

3.2.1. Deformation under different strategies of double-sided simultaneous shock. Figure 10 is the simulation result of deformation U3 of the three types of models along the Z axis. The maximum displacement of the model along the Z axis in the three ways is 0.00409mm, 0.00415mm, 0.00427mm, and the deformation is almost negligible.

The position of paths is the same as that of Figure 5. Figure 11 is a plot of displacement changes of Path 1-Path 3 under different strategies. In general, the three strategies along the Z-axis displacement U3 have little difference, and are all stable among 0.0025mm to 0.0030mm, which means that the double-sided simultaneous shock has little effect on the deformation of the edge of the model.

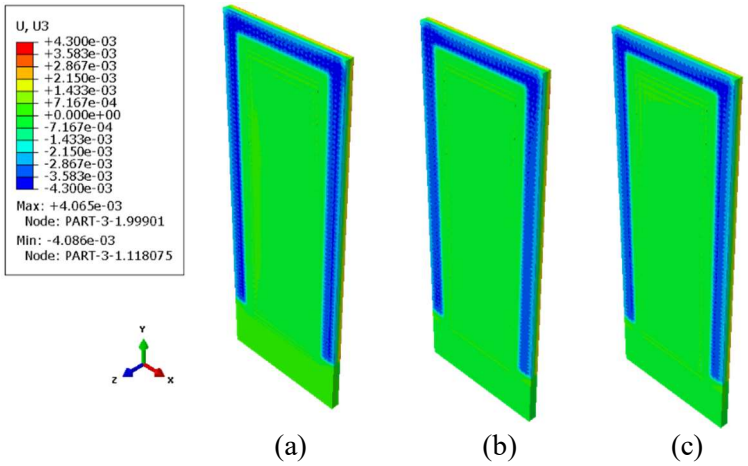

Figure 10. Z-direction deformation diagram under (a) Strategy 1, (b) Strategy 2, (c) Strategy 3.

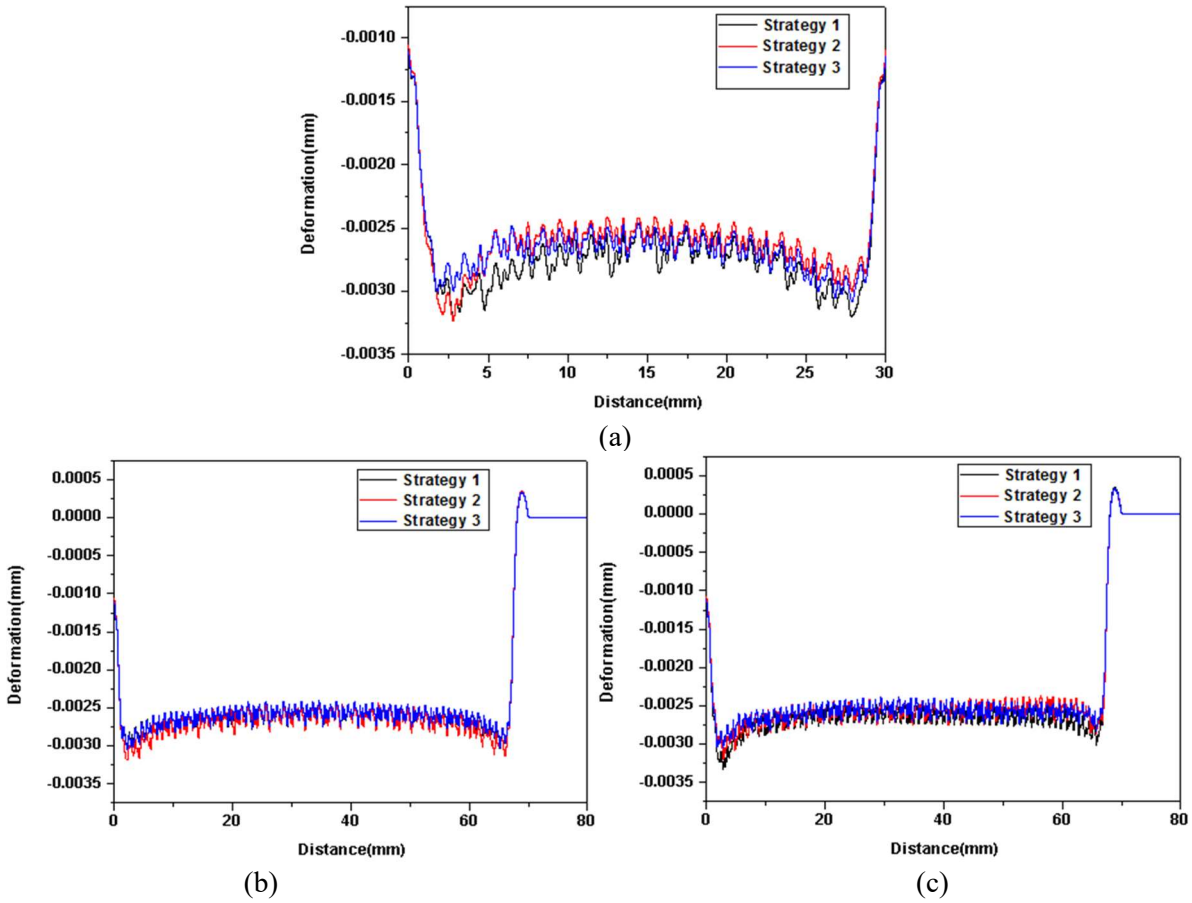

Figure 11. Displacement curves of (a) Path 1, (b) Path 2 and (c) Path 3 under different strategies.

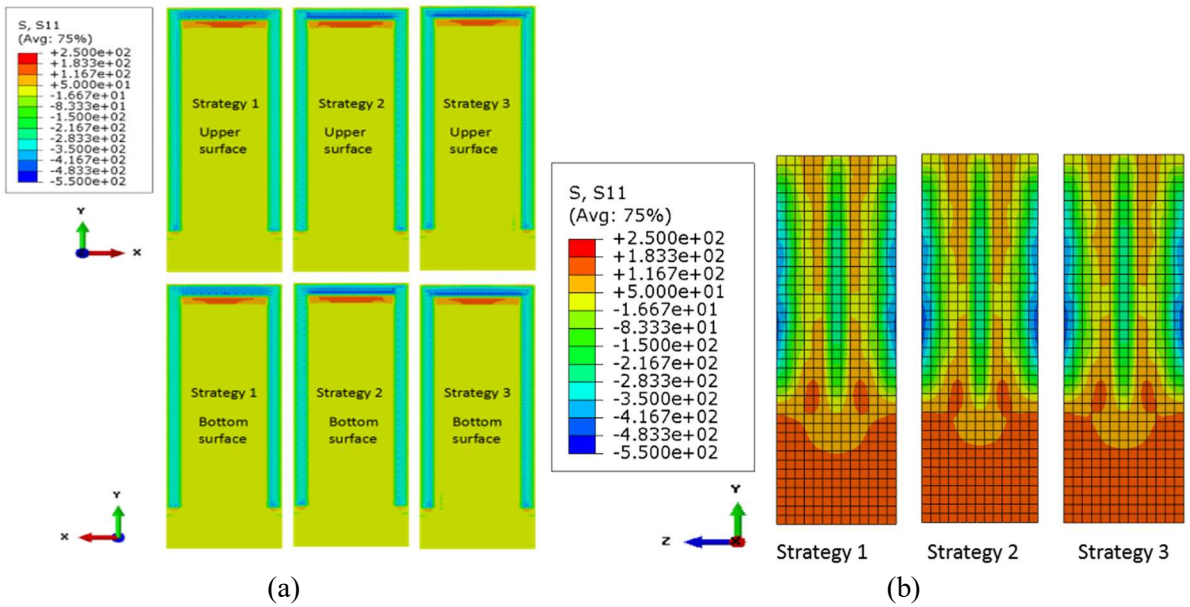

(a) (b)

Figure 12. Residual stress S11 distribution on two sides under simultaneously shock (a) Upper and lower surfaces, (b) Middle section.

3.2.2. Residual stress under different strategies of double-sided simultaneous shock. Figure 12(a) shows the simulation results of the residual stress S11 when the three shock strategies are simultaneously shocked on both sides, and Figure 12(b) shows the simulation results of the residual stress S11 of the three paths in the thickness direction of the upper portion of the model. It can be seen from the cloud diagram that large residual stresses appear in the shock regions on the upper and lower surfaces of the model. It is known from the residual stress field in the thickness direction that the upper and lower surfaces have good consistency of residual compressive stress, and there are not only residual tensile stress in the middle part of the material, but also a certain compressive stress, and the residual stress distribution is completely symmetrical. This is because stress waves are simultaneously transmitted to the middle surface of the model and overlap when double-sided shock occurs.

Figure 13 is a graph showing the residual stress of Path 4 in three strategies. It can be seen from the figure that the residual stress curve of the double-sided simultaneous shock under Path 4 is similar to that of the single-sided shock profile, but the value is increased.

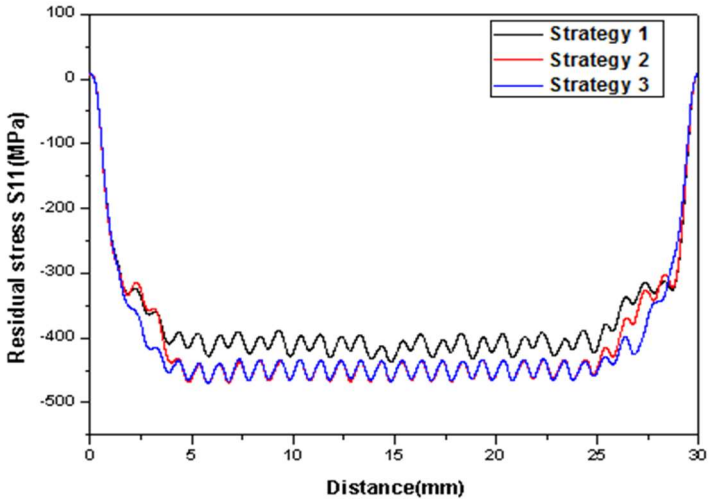

Figure 13. The residual stress curves of Path 4 under three strategies.

Table 4. Residual stress values of Path 5-Path 7 under different strategies.

Path	5			6			7		
Strategies	1	2	3	1	2	3	1	2	3
Residual stress on the upper surface(MPa)	-364	-336	-348	-400	-409	-407	-431	-457	-457
Residual stress on the lower surface(MPa)	-364	-336	-348	-400	-409	-407	-431	-457	-457

3.3. Double-sided non-simultaneous shock

3.3.1. Deformation under different strategies of double sided non-simultaneous shock. Figure 14 is a simulation result of deformation U3 of the three types of models along the Z axis. It can be seen that the displacement U3 of the model along the Z-axis increases from the bottom to the top in a wave form, and reaches a maximum value on the left and right sides of the upper surface of the model. The maximum deformations of Strategy 1, Strategy 2, and Strategy 3 are 0.1164mm, 0.1327mm, and 0.1122mm, respectively.

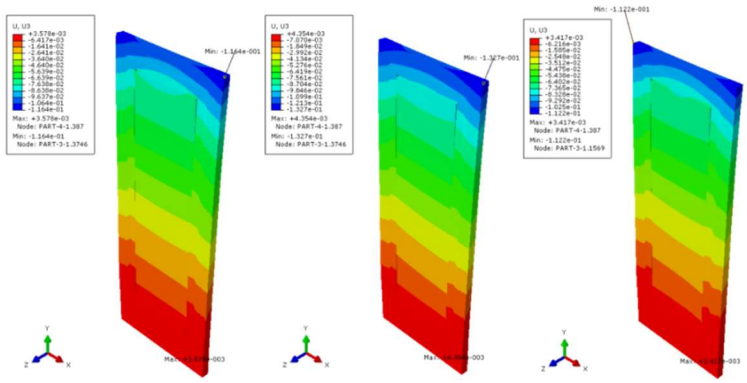

(a) (b) (c)

Figure 14. Deformation diagram under (a) Strategy 1, (b) Strategy 2, (c) Strategy 3.

Figure 15 shows the paths built and Figure 16 is a plot of the displacement of Path 1-Path 3 under different strategies. On the whole, the displacement U3 of the strategy 2 along the Z axis is the largest, the strategy is the first time, and the strategy 3 is the smallest. Strategy 1 and 2 have a large zigzag shock path in the overall shock region, and thus contribute greatly to the deformation of the upper edge of the model. Strategy 3 is a linear reciprocating shock of the overall shock region (especially parallel to the upper edge of the model), which reduces its effect on edge deformation.

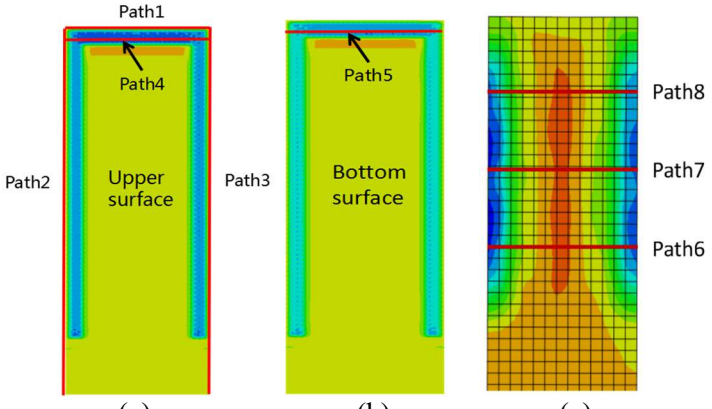

(a) (b) (c)

Figure 15. Path diagram of model (a) Upper surface path, (b) Lower surface path, (c) Middle section path.

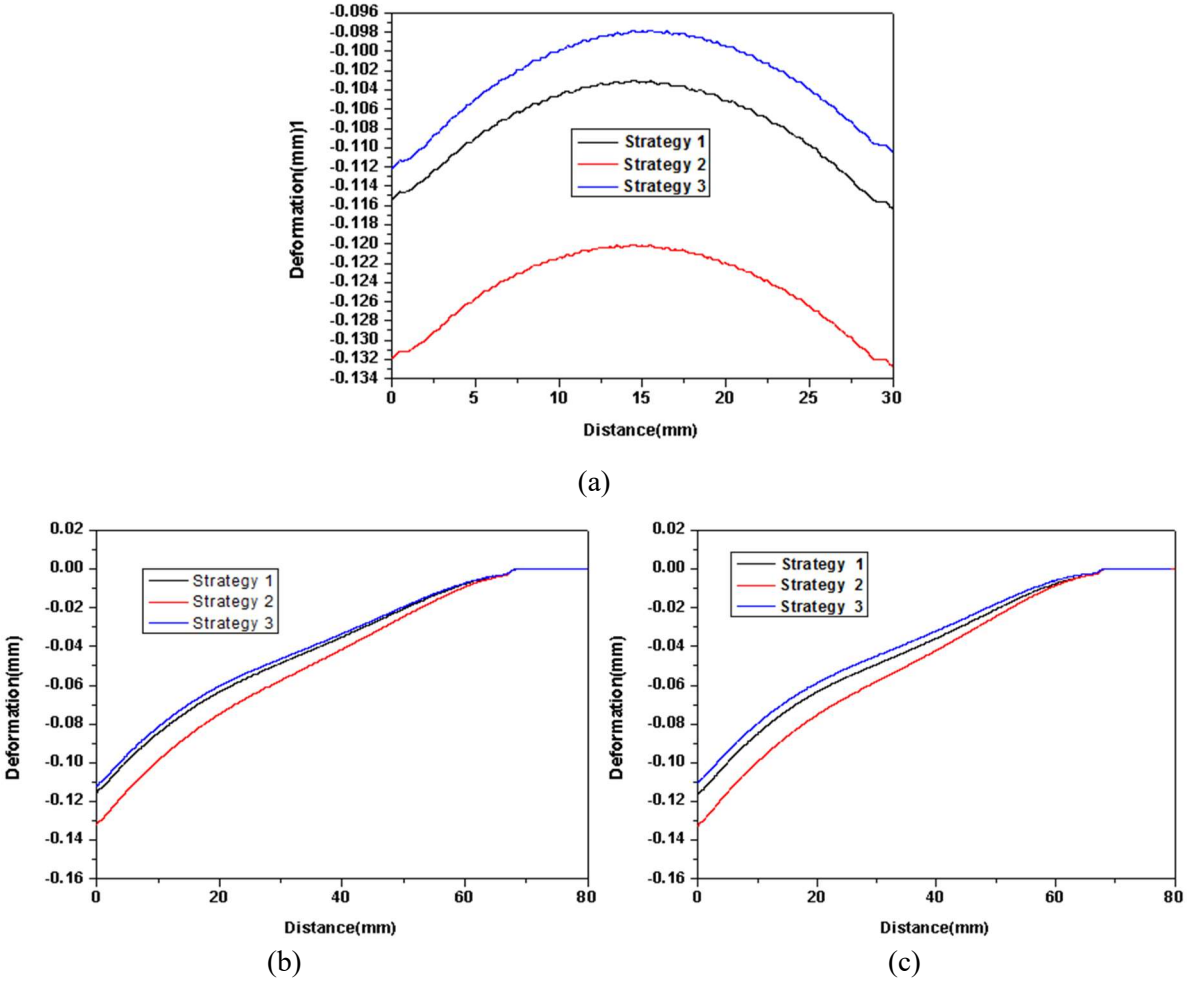

Figure 16. Displacement curves of (a) Path 1, (b) Path 2 and (c) Path 3 under different strategies.

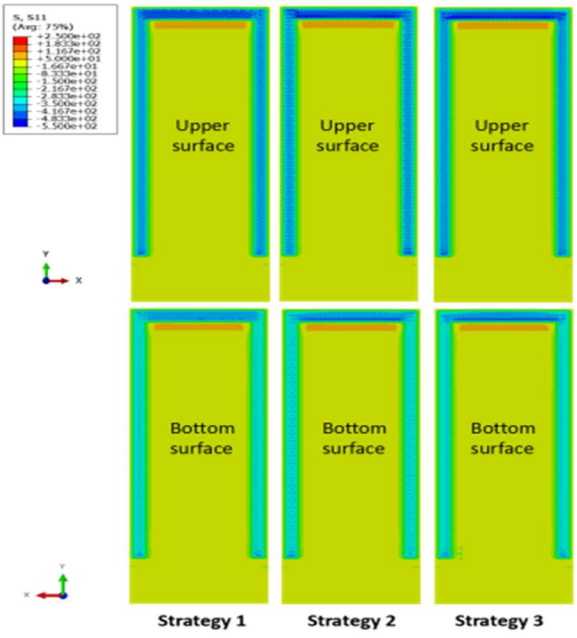

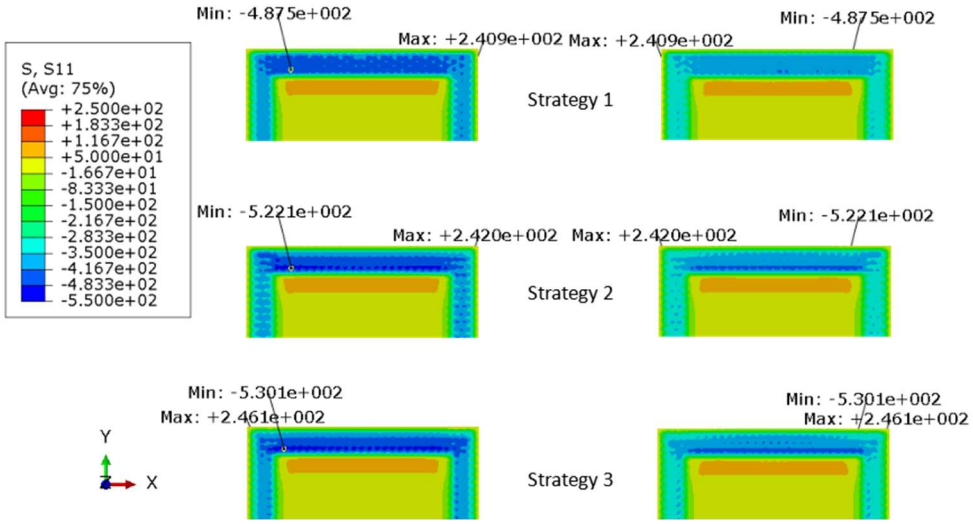

(b)

Figure 17. Residual stress S11 distribution on two sides under non-simultaneous shock (a) Overall view, (b) Partial view.

3.3.2. Residual stress under different strategies of double sided non-simultaneous shock. Figure 17(a) is the simulation result of residual stress S11 in three strategies when the two sides are not simultaneously shocking. Figure 17(b) is the simulation result of S11 amplification of the maximum residual stress. Figure 18 is the S11 simulation results of residual stresses in the middle section of the upper part of the model in the three directions along the thickness direction. It can be seen from the graph that there is obvious residual compressive stress on the upper and lower surfaces, and sandwich-like sandwich distribution appears in the thickness direction. The residual compressive stress of the upper and lower surfaces is different, and the value of the upper surface is larger than that of the lower surface, which is caused by the non-simultaneous shock: the upper surface is first shocked by laser, and the model has been restressed when the laser shock is applied to the lower surface.

Figure 19 is a graph showing residual stress changes of Path 4 and Path 5 in three strategies. It can be seen from the curve that the curves of strategy 2 and strategy 3 are similar and the waveform is relatively stable under the double-sided non-simultaneous shock, and the strategy 1 obtains a small residual stress, which is related to the manner in which the strategy 1 is jagged in the upper part of the model.

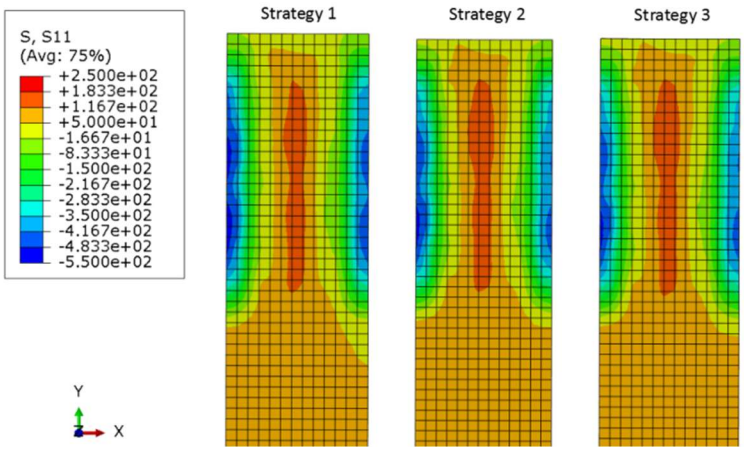

Figure 18. The distribution of the residual stress S11 in the middle section of the model in three strategies along the thickness direction.

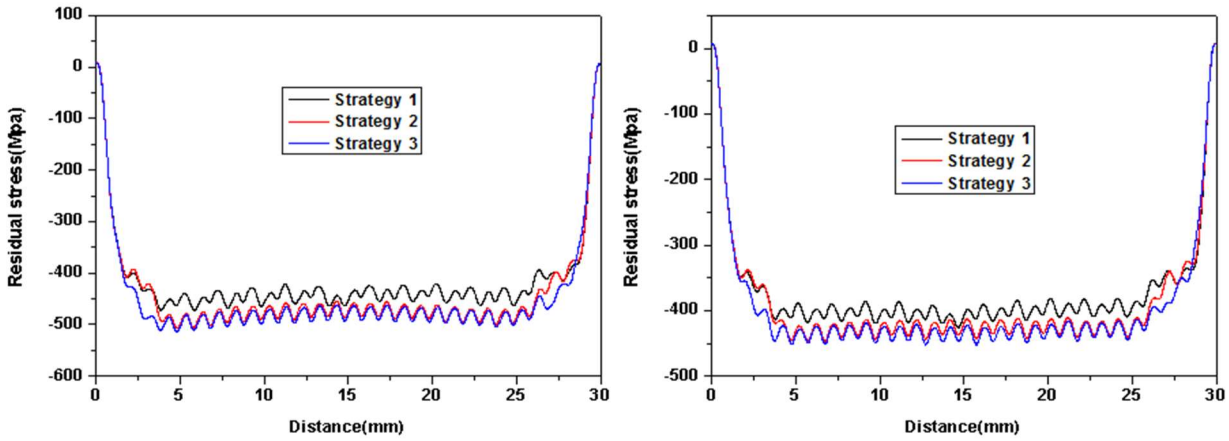

Figure 19. Residual stress curves of (a) Path 4 and (b) Path 5 in three strategies.

Table 5. Residual stress values of Path 6-Path 8 under different strategies.

Path	5			6			7		
Strategies	1	2	3	1	2	3	1	2	3
Residual stress on the upper surface(MPa)	-453	-473	-479	-442	-447	-448	-398	-382	-380
Residual stress on the lower surface(MPa)	-406	-418	-427	-391	-392	-397	-367	-353	-355

Table 5 shows the residual stress values of Path 6-Path 8 under different strategies. Comparing the residual compressive stress values at the beginning and end points on the three paths, the difference between the two is about 40~50MPa due to the existence of the restressed field at different times. For the areas near Path 6 and Path 7 with large residual compressive stress, compare the residual compressive stress of the upper and lower surfaces of the three methods, and get Strategy 3>Strategy 2>Strategy 1.

3.4. Comparative analysis of single-sided, double-sided simultaneous and double-sided non-simultaneous shock

3.4.1. Comparative analysis of deformation. Table 6 shows the deformation U3 of the model in three strategies, which are single-sided, double-sided simultaneous and double-sided non-simultaneous shock. It is found that the deformation of the single-sided shock model is larger, the maximum value is more than 1mm, and the deformation of the double-sided simultaneous shock model is small, negligible, and the deformation of the double-sided non-simultaneous shock model is between the above two.

Table 6. Maximum deformation U3 of the model in single-sided, double-sided simultaneous and double-sided non-simultaneous shock under different strategies.

	Strategy 1 mm	Strategy 2 mm	Strategy 3 mm
Single-sided,	-1.091	-1.070	-1.098
Double-sided simultaneous	-0.00409	-0.00415	-0.00427
Double-sided non-simultaneous	-0.1164	-0.1327	-0.1122

The deformation difference produced by the three strategies in the case of single-sided and double-sided simultaneous shock is small and almost negligible, the deformation caused by the double-sided non-simultaneous shock is quite different, and the strategy 3 linear reciprocating path is beneficial to

reduce Small shock deformation, and the excessive jagged path of strategy 1, strategy 2, due to the too frequent change of the shock direction, is not conducive to the control of material deformation.

3.4.2. Comparative analysis of residual stress. Table 7 shows the maximum residual compressive stress S11 of models subjected to unilateral, bilateral and bilateral non-simultaneous shock in three different ways. The maximum residual stress induced by unilateral shock is smaller than 500 MPa, and the maximum residual stress induced by double-sided shock is larger than 500 MPa. The maximum residual stress induced by double-sided non-simultaneous shock is slightly smaller than that induced by double-sided simultaneous shock.

Table 7. Maximum residual compressive stress S11 of the model in single-sided, double-sided simultaneous and double-sided non-simultaneous shock under different strategies.

	Strategy 1 MPa	Strategy 2 MPa	Strategy 3 MPa
Single-sided	-421.0	-457.0	-460.3
Double-sided simultaneous	-517.6	-538.0	-531.1
Double-sided non-simultaneous	-487.5	-522.1	-530.1

Table 8. Average value of residual compressive stress S11 of the model in single-sided, double-sided simultaneous and double-sided non-simultaneous shock under different strategies.

	Strategy 1 MPa	Strategy 2 MPa	Strategy 3 MPa
Single-sided,	-140.7	-140.4	-141.6
Double-sided simultaneous	-150.5	-151.0	-152.3
Double-sided non-simultaneous	-192.9	-192.4	-193.6

Table 8 is the average value of the residual compressive stress S11 of the shock region of the model in three strategies, which are single-sided, double-sided simultaneous, and double-sided non-simultaneous shock, respectively. The average residual stress induced by single-sided shock is smaller, both above 140 MPa. The average residual stress induced by double-sided simultaneous shock is above 150 MPa, and the residual stress induced by double-sided non-simultaneous shock is larger, both above 190 MPa.

From the above analysis, it can be seen that the different ways have a greater shock on the maximum residual stress of models, the maximum values of strategy 2 and strategy 3 are close, and significantly higher than strategy 1. The average residual stress in strategy 3 is slightly higher than that in strategy 1 and 2.

4. Conclusion

In this paper, the effects of different LSP methods on the deformation and residual stress characteristics of TC17 models are studied by finite element analysis (FEA).

The deformation on the model of double-sided simultaneous, double-sided non-simultaneous, single-sided LSP becomes larger in turn. Different shock strategies have different deformations in the case of double-sided non-simultaneous shock. Among them, the linear reciprocating path of strategy 3 is beneficial to reduce the shock deformation, while the excessive jagged path of strategy 1, and strategy 2 is not conducive to the control of material deformation.

The average residual stress induced by the single-sided, double-sided simultaneous and double-sided non-simultaneous shock in the shock region of the model becomes larger in turn, and “one-sided”, “completely symmetrical” and “sandwich” are sequentially generated in the thickness direction of the model. Residual stress distribution. The residual stress distribution generated on the surface of the model by different shock strategies is similar, and the average residual stress of the model is less affected. The

average residual stress of the strategy 3 is slightly higher than that of the strategy 1 and strategy 2; different shock strategies the maximum value of the residual stress of the model has a certain influence. The maximum values of the strategy 2 and the strategy 3 are relatively close, and are significantly higher than the strategy 1.

Double-sided simultaneous, double-sided non-simultaneous shock can achieve smaller deformation and higher residual stress than single-sided shock. The shock characteristics of strategy 3 are beneficial to reduce the deformation of the model while increasing the residual stress of the model.

Acknowledgments
This work was financially supported by the National Key Research and Development Program of China (No. 2016YFB1100202).

References

[1] YingHong Li, WeiFeng He, et al. The strengthening mechanism of laser shock processing and its application on the aero-engine components [J]. Science China Press, 2015, 45 (01): 1 - 8.
[2] Trdan U, Porro J A, Ocaña J L, et al. Laser shock peening without absorbent coatin-g (LSPwC) effect on 3D surface topography and mechanical properties of 6082-T651Al alloy [J]. Surface & Coatings Technology, 2012, 208 (6): 109 - 116.
[3] Zhang Y C. Key problems and application prospects of laser shock processing industrialization [J]. Laser & Optoelectronics Progress, 2007, 44 (3): 74 - 77.
[4] Lu J Z, Luo K Y, Dai F Z, et al. Effects of multiple laser shock processing (LSP) shocks on mechanical properties and wear behaviors of AISI 8620 steel [J]. Materials Science & Engineering A, 2012, 536 (3): 57 - 63.
[5] Liao Y L, Ye C, Kim BJ, et al. Nucleation of highly dense nanoscale precipitates based on warm laser shock peening [J]. Journal of Applied Physics, 2010, 108 (6): 063518.
[6] Qiao H C, Zhao Y X, Zhao J B, et al. Effect of laser peening on microstructures a-nd properties of TiAl alloy [J]. Optics & Precision Engineering, 2014, 22 (7): 1766 - 1773.
[7] Qiao H C, Zhao J B, Lu Y. Develop and Analysis of Nanosecond Pulse Width Nd: YAG Laser for Laser Peening [J]. Chinese Journal of Lasers, 2013, 40(8): 1-7.
[8] Zhu J, Jiao X, Zhou C, et al. Applications of Underwater Laser Peening in Nuclear Power Plant Maintenance [J]. Energy Procedia, 2012, 16: 153 - 158.
[9] Altenberger I, Nalla R K, Sano Y, et al. On the effect of deep-rolling and laser-peening on the stress-controlled low- and high-cycle fatigue behavior of Ti–6Al–4V at elevated temperatures up to 550°C [J]. International Journal of Fatigue, 2012, 44: 292-302.
[10] Sano Y, Masaki K, Gushi T, et al. Improvement in fatigue performance of friction stir welded A6061-T6 aluminum alloy by laser peening without coating [J]. Materials & Design, 2012, 36: 809 - 814.
[11] Warren A W, Guo Y B, Chen S C. Massive parallel laser shock peening: Simulation, analysis, and validation[J]. International Journal of Fatigue, 2008, 30 (1): 188 - 197.
[12] Hfaiedh N, Peyre P, Song H, et al. Finite element analysis of laser shock peening of 2050-T8 aluminum alloy[J]. International Journal of Fatigue, 2015, 70: 480 - 489.
[13] Correa C, Lara L R D, Díaz M, et al. Influence of pulse sequence and edge material effect on fatigue life of Al2024-T351 specimens treated by laser shock processing [J]. International Journal of Fatigue, 2015, 70: 196 - 204.
[14] Bhamare S, Ramakrishnan G, Mannava S R, et al. Simulation-based optimization of laser shock peening process for improved bending fatigue life of Ti–6Al–2Sn–4Zr–2Mo alloy [J]. Surface & Coatings Technology, 2013, 232 (232): 464 - 474.
[15] Shadangi Y, Chattopadhyay K, Rai S B, et al. Effect of LASER shock peening on microstructure, mechanical properties and corrosion behavior of interstitial free steel [J]. Surface & Coatings Technology, 2015, 280: 216 - 224.
[16] Lu J Z, Luo K Y, Zhang Y K, et al. Effects of laser shock processing and strain rate on tensile

property of LY2 aluminum alloy [J]. Materials Science & EngineeringA, 2010, 528 (2): 730-735.

[17] Zhang L, Luo K Y, Lu J Z, et al. Effects of laser shock processing with different shocked paths on mechanical properties of laser welded ANSI 304 stainless steel joint[J]. Materials Science & Engineering A, 2011, 528 (13–14): 4652 - 4657.

[18] Lu J Z, Zhong J S, Luo K Y, et al. Strain rate correspondence of fracture surface features and tensile properties in AISI304 stainless steel under different LSP shock time [J]. Surface & Coatings Technology, 2013, 221 (16): 88 - 93.

[19] Abrate S. Shock Dynamics[M]// Shock Engineering of Composite Structures. Springer Vienna, 2011: 71-96.

[20] Ju H K, Yun J K, Kim J S. Effects of simulation parameters on residual stresses for laser shock peening finite element analysis [J]. Journal of Mechanical Science & Technology, 2013, 27 (7): 2025 - 2034.

[21] Johnson G R, Cook W H. Fracture characteristics of three metals subjected to various strains, strain rates, temperatures and pressures [J]. Engineering Fracture Mechanic-s, 1985, 21 (1): 31 - 48.

[22] Wang, B. L, "Study on the Mechanical Properties of Titanium Alloy TC17 and Characteristics in Machining," Doctoral dissertation (Shandong University, 2013).

[23] Fabbro R, Peyre P, Berthe L, et al. Physics and applications of laser-shock processing [J]. Proceedings of SPIE - The International Society for Optical Engineering, 2000, 3888 (6): 155 - 164.

[24] Zhang W, Yao Y L, Noyan I C. Microscale Laser Shock Peening of Thin Films, Part 1: Experiment, Modelling and Simulation [J]. Journal of Manufacturing Science &Engineering, 2004, 126 (1): 10 - 17.